








# Erythrocyte sedimentation: Effect of aggregation energy on gel structure during collapse

Anil Kumar Dasanna <sup>1</sup>, Alexis Darras <sup>2,\*</sup>, Thomas John <sup>2</sup>, Gerhard Gompper <sup>1</sup>, Lars Kaestner <sup>2,3</sup>,  
Christian Wagner <sup>2,4</sup> and Dmitry A. Fedosov <sup>1</sup>

<sup>1</sup>*Theoretical Physics of Living Matter, Institute of Biological Information Processing and Institute for Advanced Simulation, Forschungszentrum Jülich, 52425 Jülich, Germany*

<sup>2</sup>*Experimental Physics, Saarland University, 66123 Saarbrücken, Germany*

<sup>3</sup>*Theoretical Medicine and Biosciences, Saarland University, 66424 Homburg, Germany*

<sup>4</sup>*Department of Physics and Materials Science, University of Luxembourg, L-1511 Luxembourg City, Luxembourg*



(Received 23 July 2021; accepted 2 February 2022; published 23 February 2022)

The erythrocyte (or red blood cell) sedimentation rate (ESR) is commonly interpreted as a measure of cell aggregation and as a biomarker of inflammation. It is well known that an increase of fibrinogen concentration, an aggregation-inducing protein for erythrocytes, leads to an increase of the sedimentation rate of erythrocytes, which is generally explained through the formation and faster settling of large disjoint aggregates. However, many aspects of erythrocyte sedimentation conform well with the collapse of a particle gel rather than with the sedimentation of disjoint aggregates. Using experiments and cell-level numerical simulations, we systematically investigate the dependence of ESR on fibrinogen concentration and its relation to the microstructure of the gel-like erythrocyte suspension. We show that for physiological aggregation interactions, an increase in the attraction strength between cells results in a cell network with larger void spaces. This geometrical change in the network structure occurs due to anisotropic shape and deformability of erythrocytes and leads to an increased gel permeability and faster sedimentation. Our results provide a comprehensive relation between the ESR and the cell-level structure of erythrocyte suspensions and support the gel hypothesis in the interpretation of blood sedimentation.

DOI: [10.1103/PhysRevE.105.024610](https://doi.org/10.1103/PhysRevE.105.024610)

## I. INTRODUCTION

The erythrocyte sedimentation rate (ESR) is a common blood test that measures how fast red blood cells (erythrocytes) settle at the bottom of a test tube that contains an anti-coagulated but undiluted blood sample, composed of cells and blood plasma as carrier liquid. It is one of the oldest nonspecific medical tests for inflammation and is still a gold standard for diagnosis and monitoring of inflammatory diseases [1,2]. Its first description dates back to the 19th century, but a similar procedure was already in use by ancient Greeks [3].

Interestingly, the sedimentation rate is usually much faster than one would expect from the sedimentation of a single cells in a highly diluted sample. A common physical interpretation of the ESR is that erythrocytes suspended in blood plasma sediment as separate large aggregates, which is amenable to a theoretical description using the Stokes law for the drag force [4–9]. However, the state of the art indicates that particle suspensions with a high volume fraction of weakly attractive particles form a percolating network, which is generally referred to as a gel [10–19].

In the joint letter [20], we have demonstrated that sedimenting erythrocytes at high volume fractions indeed also

form a gel, which explains pertinent features of the sedimentation process and leads to a consistent theoretical description of sedimentation dynamics. An interesting observation for blood sedimentation is that the ESR increases with increasing the attraction between suspended cells [5,21]. This is exactly opposite to the behavior of hard-particle suspensions, where an increase in attractive interactions between particles results in gel stabilization, which can significantly delay and slow down the sedimentation process [12,17,21–26]. This observation is of particular importance for medical applications which generally use the ESR as an inflammation marker. The current rationale for this marker is that inflammation correlates with high fibrinogen levels, which enhances the aggregation of erythrocytes. Therefore, a faster ESR for stronger aggregation interactions is believed to be related to the aggregation-mediated formation of large separate aggregates, whose sedimentation is faster in the Stokes regime [27,28]. The dependence of ESR on fibrinogen concentration is illustrated in Fig. 1.

To systematically investigate the behavior of ESR on fibrinogen concentration and its relation to the microstructure of erythrocyte suspension, we employ a combination of experiments and numerical simulations. We show that, in contrast to classical hard-particle suspensions [17–19], an increase in attraction strength between cells significantly modifies the structure and permeability of erythrocyte gel, resulting in a faster ESR. This sedimentation behavior is due to the characteristic discocyte shape of erythrocytes and their membrane

\*alexis.charles.darras@gmail.com

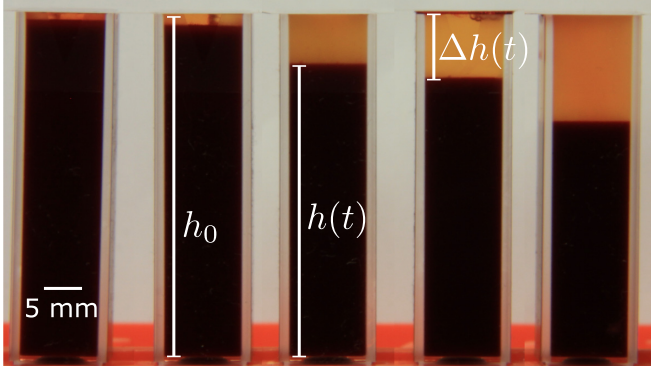


FIG. 1. ESR experiments. Cuvettes containing blood samples with various levels of fibrinogen are shown after 2 hours at rest. Hematocrit (i.e., erythrocyte volume fraction) in all containers has been adjusted to  $\phi = 0.45$ . The very left container corresponds to erythrocytes suspended in autologous serum (no fibrinogen), while the very right contains erythrocytes in autologous blood plasma (maximum amount of fibrinogen). Middle containers contain cells suspended in a mixture of serum and plasma, with volume proportions of 25%, 50%, and 75% of plasma, from left to right. The various height characteristics ( $h_0$ ,  $h(t)$  and  $\Delta h(t)$ ) are also indicated.

flexibility. The discocyte geometry facilitates the formation of well-known rouleaux stacks, which are eventually arranged into a network-like structure. More importantly, the deformability of red blood cells (RBCs) implies an increase in ESR at high fibrinogen concentrations, as simulations demonstrate that the dependence of ESR on the attraction strength nearly disappears for stiff erythrocytes. These results provide a consistent explanation for the behavior of ESR as a function of fibrinogen concentration and further support the gel hypothesis for erythrocyte suspensions.

The paper is organized as follows. Section II summarizes the theoretical model for gel permeability and dynamic sedimentation introduced in the joint letter [20], since changes in the associated model parameters form a basis for the analysis of presented data. Experimental and numerical methods are given in Sec. III. Section IV presents the dependence of sedimentation on fibrinogen concentration from experimental measurements, along with its correlation with the microstructure of erythrocyte suspensions.

## II. THEORETICAL DESCRIPTION OF SEDIMENTATION

We start with a brief summary of the theoretical model for gel structure and permeability developed in the joint letter [20], since model parameters are frequently used in data analysis. To describe the gravitational collapse of erythrocyte gel, a time-dependent volume fraction  $\phi(t)$  is considered, covering the range from dilute to close-packed cell suspensions. For simplicity, we assume that only gravitational forces drive gel sedimentation, and a Carman-Kozeny relationship with the maximal volume fraction  $\phi_m$  smaller than unity is used to approximate gel permeability [29–33]. The characteristic velocity for the gravitational collapse of an erythrocyte suspension is obtained on the basis of Darcy's law for the flow of

a fluid through a porous medium as

$$-\frac{dh}{dt} = \frac{\Delta\rho g a^2 (\phi_m - \phi)^3}{\kappa_0 \eta \phi(1 - \phi)}, \quad (1)$$

where  $h(t)$  is the height of the gel at time  $t$ ,  $\Delta\rho$  is the density difference between erythrocytes and blood plasma,  $g$  is the gravitational acceleration,  $\eta$  is the viscosity of the suspending liquid,  $a$  is the characteristic size of pores within the gel structure, and  $\kappa_0$  is the dimensionless scaling constant of the Carman-Kozeny relationship. Here the conservation of the volume of erythrocytes provides the necessary relation between the height  $h$  and the volume fraction  $\phi$  via  $h(t)\phi(t) = h_0\phi_0$ , where  $h_0$  and  $\phi_0$  are the initial height and volume fraction at  $t = 0$ , respectively. A typical size of  $a = Rr_{\text{RBC}}$  is considered, where  $r_{\text{RBC}} = 4 \mu\text{m}$  is the average radius of an erythrocyte and  $R$  is a parameter reflecting the ratio between the size of erythrocytes and a characteristic size of fluid channels within the gel [12,18,19]. The density difference is approximately  $\Delta\rho \approx 80 \text{ kg/m}^3$  [34,35]. Starting from the initial conditions for the height  $h_0$  and volume fraction  $\phi_0$ , and taking into account the usual delay time  $t_0$  for the gel collapse [12,14,26], the height of the gel as a function of time becomes

$$h(t) = \begin{cases} h_0, & \text{if } t < t_0 \\ f^{-1}\left(f(h_0) - \frac{G\phi_m^3}{\gamma}(t - t_0)\right) & \text{if } t \geq t_0 \end{cases}, \quad (2)$$

where  $G = \Delta\rho g r_{\text{RBC}}^2 / (\eta\phi_0 h_0)$  is proportional to the inverse characteristic time for the sedimentation of single cells, and  $\gamma = \kappa_0 / R^2$  is a dimensionless fit parameter related to a characteristic time of the system. The third parameter  $\phi_m$  of this model is also included in the function  $f$ , obtained as

$$f(x) = \log(\phi_m x - \phi_0 h_0) + \frac{\phi_0 h_0 [\phi_0 h_0 (3 - \phi_m) - 2(2 - \phi_m)\phi_m x]}{2(\phi_0 h_0 - \phi_m x)^2}. \quad (3)$$

It is instructive to consider the asymptotic behavior of the time dependence of  $h(t)$  for small and large volume fractions, corresponding to short and large times, respectively. An expansion of the right-hand side of Eq. (1) for small  $\phi$  yields the behavior

$$\Delta h = h_0 - h(t) \approx h_0 [1 - \exp(-(t - t_0)/t^*)] \quad (4)$$

with the characteristic timescale  $t^* = \gamma / (G\phi_m^3)$ , while small  $\delta\phi = \phi - \phi_m$  yields to

$$\delta h(t) = h(t) - h_m \approx h_m \left(\frac{t}{t^*}\right)^{-1/2} \sqrt{\frac{1 - \phi_m}{2}} \quad (5)$$

where  $h_m$  is the height corresponding to  $\phi_m$ .

The comparison of erythrocyte sedimentation under different conditions includes the three fitting parameters: the maximum volume fraction  $\phi_m$ , the dimensionless characteristic collapse time  $\gamma$ , and the delay time  $t_0$  of the gel. The dependence of these parameters on the fibrinogen concentration, which modifies the aggregation strength between erythrocytes, will be presented, and the behavior of  $\gamma$  with respect to the aggregation strength will be discussed.

### III. METHODS

#### A. Macroscopic measurements of sedimentation

Blood samples were collected from healthy volunteers after an informed consent, in compliance with the declaration of Helsinki, as approved by the Ärztekammer des Saarlandes, ethics votum 51/18.

The sedimentation process is monitored by taking an image sequence of a translucent cuvette containing blood with a frame rate of one frame per minute (see Fig. 1 for an example of the pictures). The cuvette has an inner square cross section of 10 mm  $\times$  10 mm and a height of 40 mm. In all investigations, the interface is sharp. The height of the packed erythrocyte phase is determined using a custom written Matlab code, as follows. The image is first binarized with the Otsu threshold, using the difference between the red and the blue channels as intensity. The binarized image is then averaged horizontally to obtain an intensity profile with minimal noise. The position of the interface is then determined as the position of the maximum intensity gradient. The pixel resolution leads to a spatial accuracy of approximately 0.1 mm.

Sedimentation recordings are performed for different levels of fibrinogen, in order to quantify its effect on the parameters of the theoretical model. We focus on fibrinogen because it is one of the most efficient aggregation-promoting agents of erythrocytes [36,37]. The aggregation energy between erythrocytes, defined as the work required to separate two aggregated cells, is known to increase linearly with fibrinogen concentration for a wide range of concentrations, in contrast to some other aggregation-inducing molecules such as Dextran [36,38]. The initial volume fraction of cells was always kept at  $\phi_0 = 0.45$ , independently of fibrinogen concentration. To closely approximate physiological conditions, red blood cells (RBCs) are suspended into well-controlled mixtures of autologous blood plasma and serum. Serum can be considered as plasma without fibrinogen, as the coagulation cascade occurs during serum extraction [39,40]. The concentration of fibrinogen along with other usual blood plasma parameters was measured by standard methods in the Clinical Chemistry Laboratory of Saarland University Hospital (Homburg, Germany).

#### B. Microscopic cell structures

To rationalize dependencies of the macroscopic sedimentation parameters on the fibrinogen concentration, experiments, and numerical simulations characterizing the microscopic structure of the gel are performed.

##### 1. Experiments with quasi-2D sedimented structures

To assess structural properties of aggregated erythrocytes as a function of aggregation strength (or equivalently fibrinogen concentration), erythrocytes were allowed to settle in a pillbox-shaped microscope chamber with an inner diameter of 5 mm and a height of 1.5 mm. The initial volume fraction of 0.3% was selected very low, but high enough such that after sedimentation, a quasi-2D percolating aggregate is formed at the bottom of the chamber. Note that for these experiments, phosphate-buffered saline (PBS) solutions with fibrinogen (from 0 to 550 mg/dl) were used instead of the

plasma-serum mixture, in order to minimize possible donor-based variabilities. Fibrinogen used was from human plasma, provided by Sigma-Aldrich (St. Louis, Missouri, USA) as a powder stabilized with NaCl, and the required amount of distilled water was incorporated to the solutions to adjust osmolarities of the suspension to 290 mOsm. The final hematocrit of a 8- $\mu$ m-thick monolayer of erythrocytes at the chamber bottom is approximately  $\phi = 0.56$ , which provides a reasonable approximation for the hematocrit of the quasi-2D layer of erythrocyte gel.

##### 2. Numerical simulations: Model and methods

Since the properties of percolating networks are known to depend on the dimensionality and the underlying particle characteristics [17,19,41], numerical simulations are employed to support the interpretation of the experiments and to characterize the structure of erythrocyte gels in three dimensions during sedimentation. Simulations of blood sedimentation are performed using a mesoscopic coarse-grained model of RBCs [42–44]. Each RBC is represented by a triangulated surface with  $N_v = 500$  vertices, whose total potential energy consists of in-plane elastic energy, bending energy, surface area, and volume constraints as

$$U_{\text{tot}} = U_{\text{elastic}} + U_{\text{bend}} + U_{\text{area}} + U_{\text{vol}}. \quad (6)$$

The elastic energy  $U_{\text{elastic}}$  is a sum of attractive wormlike-chain and repulsive potentials over all network edges  $N_e$

$$U_{\text{elastic}} = \sum_{i=1}^{N_e} \left[ \frac{k_B T \ell_m (3x_i^2 - 2x_i^3)}{4p(1 - x_i)} + \frac{k_p}{\ell_i} \right], \quad (7)$$

where  $p$  is the persistence length,  $\ell_i$  is the length of edge  $i$ ,  $\ell_m$  is the maximum edge extension, and  $x_i = \ell_i / \ell_m$ . In the second term,  $k_p$  is the nonlinear spring constant of the repulsive force coefficient, defined as a power function [43,44].

The bending energy

$$U_{\text{bend}} = \sum_{i=1}^{N_e} \kappa [1 - \cos(\theta_i - \theta_0)] \quad (8)$$

describes the cost of membrane deformations due to curvature elasticity. Here  $\kappa$  is the bending rigidity,  $\theta_i$  is the angle between two adjacent faces at the edge  $i$ , and  $\theta_0$  represents the spontaneous curvature.

The third and fourth terms in Eq. (6) correspond to constraints for surface area (both local and global) and volume and are expressed as

$$U_{\text{area}} = \frac{k_a (A - A_0)^2}{2A_0} + \sum_{i=1}^{N_f} \frac{k_d (A_i - A_i^0)^2}{2A_i^0},$$

$$U_{\text{vol}} = \frac{k_v (V - V_0)^2}{2V_0}, \quad (9)$$

where  $k_a$ ,  $k_d$ , and  $k_v$  are local area, total surface area, and volume constraint coefficients, respectively.  $N_f$  is the number of faces,  $A_i$ ,  $A$ , and  $V$  are the instantaneous area of face  $i$ , total area, and volume, respectively, and the quantities with a zero subscript or superscript represent their targeted values.

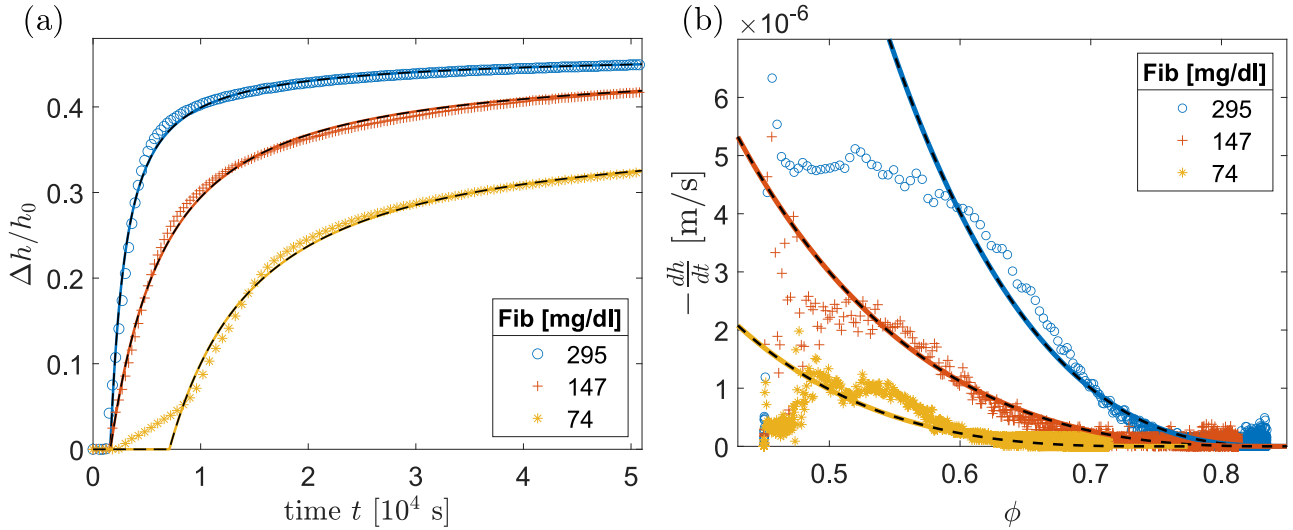


FIG. 2. (a) Time dependence of height of the interface between dense erythrocyte suspension and cell-free plasma, for various fibrinogen concentrations. The curves show the relative variation  $\Delta h/h_0 = [h_0 - h(t)]/h_0$  which corresponds to the height of the cell-free plasma layer. The symbols are experimental data, while the curves are fits from the theoretical model for  $h(t)$  in Eq. (2). (b) Associated interface speed as a function of the volume fraction  $\phi(t) = \phi_0 h_0/h(t)$ . The symbol data are computed from a smoothing spline of the  $\Delta h$  measurements, while the curves correspond to the expected speed from the fit parameters in Eq. (1).

Aggregation interactions between RBC membranes is implemented via the Lennard-Jones potential

$$U_{\text{LJ}} = \begin{cases} 4\epsilon \left[ \left( \frac{\sigma}{r} \right)^{12} - \left( \frac{\sigma}{r} \right)^6 \right] & \text{for } r < r_c \\ 0 & \text{for } r \geq r_c, \end{cases} \quad (10)$$

where  $\epsilon$  is the aggregation strength and  $\sigma = 0.6 \mu\text{m}$  characterizes the excluded-volume distance between RBCs. Here the distance  $\sigma$  is essentially determined by the resolution of the membrane discretization, i.e., the bond length of the membrane triangulation. A RBC model based on the actual structure of the lipid bilayer and the glycocalyx would be extremely expensive computationally (it would require approximately a  $10^4$  higher, since the total thickness of both layers is around 10 nm [45,46]). This cost would not allow simulations with such a large number of erythrocytes as considered here. The cutoff distance  $r_c$  is selected to be  $1.2 \mu\text{m}$ . To calibrate the aggregation strength  $\epsilon$ , several simulations are performed, in which two RBCs are first placed close to each other and let to aggregate. Then these RBCs are pulled apart with a force applied in the normal direction until they detach from each other, so that the force required for their detachment is determined [47]. For aggregation forces between two RBCs in the range of 2–6 pN,  $\epsilon$  value is in the range of  $2\text{--}5 k_B T$  (e.g.,  $F_{\text{detach}} \simeq 3.6$  pN for  $\epsilon = 2.5 k_B T$  and  $F_{\text{detach}} \simeq 6$  pN for  $\epsilon = 4.4 k_B T$ ). Such aggregation forces are similar to those measured experimentally in autologous blood plasma with optical tweezers [48]. In such conditions, the total aggregation energy between two cells in the simulations is then of the order of  $F_{\text{detach}} \sigma \sim 6 \cdot 10^2 \text{--} 9 \cdot 10^2 k_B T$ .

In simulations, a fixed number of RBCs (depending on hematocrit) is distributed in a fluid within a simulation domain of  $(50 \mu\text{m})^3$  with periodic boundary conditions in all directions. The fluid is modeled by the smoothed dissipative particle dynamics (SDPD) method, which is derived through a Lagrangian discretization of the Navier-Stokes

equations [49,50]. The choice of these boundary conditions and the fluid model is motivated by previous studies, which show that relevant collapse mechanisms for macroscopic samples are observed only with hydrodynamic interactions in bulk systems [51–53]. RBC properties correspond to average characteristics of a healthy RBC with a membrane area  $A_0 = 133 \mu\text{m}^2$ , cell volume  $V_0 = 93 \mu\text{m}^3$ , shear modulus  $\mu = 4.8 \mu\text{N/m}$ , and bending rigidity  $\kappa = 70 k_B T = 3 \times 10^{-19} \text{ J}$  [54–56]. This leads to a RBC reduced volume of  $V^* = 6V_0/(\pi D_r^3) \approx 0.64$ , where  $D_r = \sqrt{A_0/\pi} = 6.5 \mu\text{m}$  is the effective RBC diameter. Note that the stress-free shape of a RBC elastic network is assumed to be the biconcave shape of a RBC with  $V^* = 0.64$ . In addition to aggregating RBC suspensions, several cases without aggregation interactions are also considered by setting  $r_c = 2^{1/6} \sigma$  such that only repulsive forces between RBC vertices are present.

To mimic cell sedimentation, a constant force  $F_{\text{RBC}}$  is applied to all membrane vertices of RBCs along the negative  $z$  direction, and force  $F_{\text{fl}}$  in the opposite direction is applied to all fluid particles. Since the numbers of RBC vertices and fluid particles differ, the forces applied on each type of particles are also different. However, the total force in the simulation domain remains zero. In this way, the flow resistance, or permeability, of porous-like RBC structures for different simulation parameters can be measured. The pressure difference over height  $z$  can be calculated as  $\Delta P/z = \rho_{\text{RBC}} F_{\text{RBC}} - \rho_{\text{fl}} F_{\text{fl}}$ . This pressure difference results in a net sedimentation velocity  $v = v_{\text{RBC}} - v_{\text{fl}}$ . The permeability  $k$  of the RBC structure is then derived through Darcy's law as  $k = (1 - \phi)v\eta/\frac{\partial P}{\partial z}$ .

It is important to note that we are considering here the case of small sedimentation velocities, so that the shape of individual RBCs is only weakly affected by the flow forces [57]. An illustrative movie from the simulations can be found as Supplemental Movie S1 [58].

In the theoretical model of the joint letter [20], this permeability is assumed to be related to the structure of the pore size



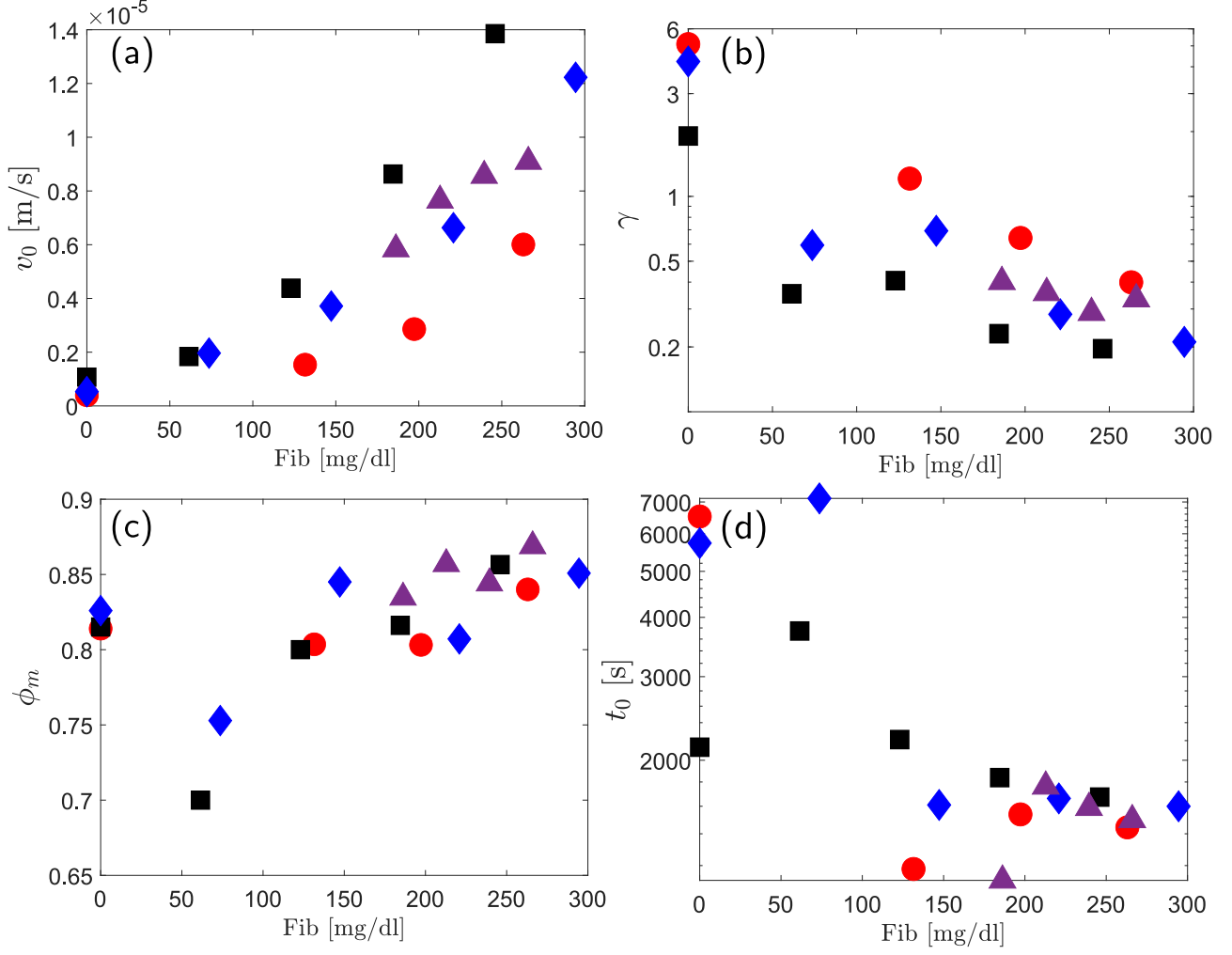


FIG. 3. Dependence of the model parameters on the fibrinogen concentration for different blood donors. Different symbols and colors indicate different donors. (a) Initial sedimentation velocity at  $t_0$  computed using Eq. (1) with  $\phi = \phi_0 = 0.45$ . (b) Dimensionless characteristic time  $\gamma$  of the sedimentation process. (c) The final volume fraction  $\phi_m$ . (d) The delay time  $t_0$  before the sedimentation starts.

$a$  of the RBC structure through a modified Carman-Kozeny relationship:  $k = \frac{1}{\kappa_0} \frac{a^2(\phi_m - \phi)^3}{\phi^2}$ . The calculation of characteristic pore sizes which determine the permeability of suspended RBC structures is performed as follows. For each simulation trajectory, we take multiple  $xy$  slices (at constant  $z$ ) over several time intervals. For each slice, multiple straight lines are drawn in the  $x$  and  $y$  directions. The lengths of these lines outside the RBCs determine the lengths of void spaces and their average provide an estimation of the pores mean chord length, which corresponds to an average pore size (see Supplemental Fig. 3 for illustration [58]). We focused on the  $xy$  plane, since the flow during sedimentation is mainly directed along the  $z$  axis, implying that the characteristic length for the shear stress is the one in the  $xy$  plane. Supplemental Fig. 4 compares the obtained values in  $xy$  and  $xz$  planes.

The choice of a different method for the determination of characteristic pore sizes has been determined mainly by the difference in dimension between the observations in experiments and in simulations. In experiments we observe areas of  $500 \text{ m} \times 400 \text{ m}$ , while the simulation domain is only  $50 \text{ m} \times 50 \text{ m}$ , i.e., around 100 times smaller. In the experiments,

we observe enough holes not touching the border of the pictures to perform statistics based on single-hole properties. For simulations, only a few holes are observed in each cut, and the biggest holes are truncated by the simulations borders, often not allowing us to compute hole areas. The statistics performed offers an estimation of the mean chord length (which is one of the usual tools to characterize percolating structures; see, e.g., [12]), which presents more robust statistics.

In addition to the aforementioned measurements, we also characterized the percolation probability within the numerical simulations, since this percolation is a prerequisite of the macroscopic model [Eq. (1)]. Those results are discussed in the Supplemental Material [58]; see also Ref. [59–61].

## IV. RESULTS

### A. Macroscopic sedimentation measurements

Figure 2(a) shows the time dependence of the erythrocyte column height during the sedimentation process for various levels of fibrinogen. The sedimentation of erythrocytes

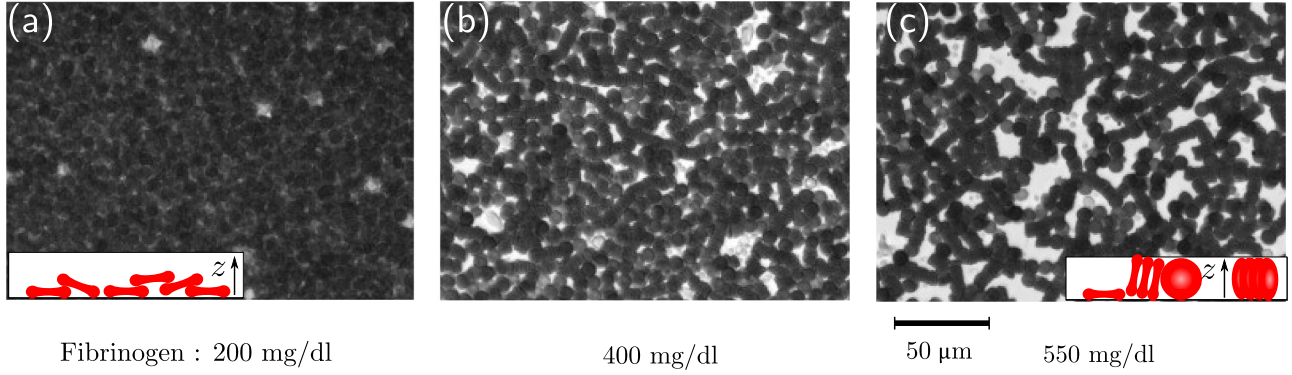


FIG. 4. Pictures of 2D cell networks obtained for various fibrinogen concentrations in PBS, after sedimentation to the bottom of a microscopy chamber. The final hematocrit at the bottom of the chamber within a  $8\text{ }\mu\text{m}$  height monolayer of erythrocytes is equal to approximately  $\phi = 0.56$ . Qualitative differences in aggregate geometries and characteristic sizes of the pores are clearly visible for different fibrinogen concentrations. Insets in (a) and (c) are schemes of the  $xz$  plane in the quasi-2D experiments, for both minimal (a) and maximal (c) fibrinogen concentration. Although the volume fraction is the same for each measurement, the total 2D pore area in the  $xy$  plane increases from (a) to (c) because more cells are seen from the side when incorporated in a rouleau, while most of the cells lie flat at the bottom of the container in (a).

becomes slower when the concentration of fibrinogen decreases. The lines in Fig. 2(a) represent the corresponding fits using the theoretical model from Eq. (2). (Corresponding fit parameters, for the respective fibrinogen concentrations of {74, 147, 295} mg/dl are  $\gamma = \{0.59, 0.69, 0.21\}$ ,  $\phi_m = \{0.75, 0.845, 0.85\}$ , and  $t_0 = \{7.1, 1.6, 1.6\} \times 10^3$  s, respectively.) The theoretical curves generally show a good agreement with experimental data, except at short times when the sedimentation starts. The beginning of sedimentation is not well captured by our model, because gels may require some structural rearrangements (e.g., dynamic formation of fluid channels) before macroscopic sedimentation can be observed [14,18,19]. For instance, the curve with fibrinogen concentration 74 mg/dl exhibits first a slow sedimentation velocity, which then suddenly increases. Presumably, a slow settling of the gel occurs before larger fluid channels appear and significantly accelerate sedimentation in some cases [18]. In this respect, the delay time  $t_0$  characterizes the time required for cells to reorganize and establish dynamic fluid channels which enable fast sedimentation [12–16].

Figure 2(b) presents sedimentation velocities as a function of calculated  $\phi(t)$  from height measurements for different fibrinogen concentrations. The speed of the interface between dense erythrocyte suspension and the cell-free plasma extracted from experimental measurements (symbols) show strong fluctuations, especially at the beginning of the sedimentation process or when  $\phi \sim \phi_0$ . However, we slightly smoothed the experimental data to calculate the numerical derivative. As a result we obtain speeds that follow well the average trend given by the theoretical curves of  $dh/dt$  from Eq. (1).

As mentioned before, Eq. (2) allows the extraction of the model parameters from sedimentation experiments, which are shown in Fig. 3 along the initial speed of the interface between packed erythrocytes and the cell-free plasma. Data from various donors are shown with different symbols and colors. The initial sedimentation speed  $v_0$  right at the beginning of the sedimentation process (i.e., at  $\phi = \phi_0 = 0.45$ ) increases with an increase in the fibrinogen concentration [see Fig. 3(a)].

Here Eq. (1) is employed to compute  $v_0$  instead of raw data because the relative variation in the instant velocity is of the order of magnitude of the slowest velocities observed. Even though there is some variation in  $v_0$  for different donors, the common trend of increasing  $v_0$  with fibrinogen concentration remains consistent. These donor-related differences are likely due to differences in the concentration of other blood proteins beside fibrinogen, since they also influence RBC aggregation and sedimentation properties, but to a smaller extent.

Consistently with the velocity increase, the dimensionless characteristic time  $\gamma$  of sedimentation in Fig. 3(b) decreases overall with increasing fibrinogen concentration. This can be rationalized by the fact that characteristic channel sizes (i.e., the parameter  $R$  in the model) within erythrocyte structures become larger with increasing fibrinogen concentration, as will be shown later.

Figure 3(c) shows that the final volume fraction  $\phi_m$  of sedimented erythrocytes is nearly independent of fibrinogen concentration and mostly lies within the range of  $0.84 \pm 0.05$ . A very slight increase in  $\phi_m$  with the fibrinogen concentration implies that an increasing attraction strength generates a slightly better compaction of flexible cells. However, this trend is within the order of the variations found for various donors, and further measurements would be required to rigorously support such a trend. In any case, changes in  $\phi_m$  cannot explain the observed variations in the sedimentation velocity for different donors.

Surprisingly, the delay time  $t_0$  in Fig. 3(d) decreases with increasing fibrinogen concentration. Given that the delay time is usually related to the coarsening of particle gel [12,26], this seems to indicate that stronger attractive interactions lead to faster rearrangement of initial erythrocyte structures towards the establishment of fluid channels. Interestingly, the dependence of  $t_0$  on particle interactions is exactly opposite for suspensions of the isotropic hard sphere, where a strong attraction stabilizes such gels [12,14]. In these studies, the main proposition is that  $t_0$  characterizes the time required to break existing “bonds” within an initially stable gel. This appears to

be different for a suspension of RBCs, where attractive interactions are associated with accelerated apparition of vertical channels within the RBC gel. Therefore, we hypothesize that the flexibility and/or anisotropy of RBCs causes a change in the dependence of  $t_0$  on intercell attractive interactions. Preliminary measurements supporting this claim are available in the Supplemental Material [58]. We can also partially exclude the diffusion-limited process of initial structure formation, as it is expected to occur on a significantly shorter timescale than the delay time  $t_0$ . For example, the characteristic time for doublet formation by diffusion-limited aggregation can be estimated as  $t_D = \pi r_{\text{RBC}}^3 \eta / (\phi k_B T) \sim 10^2$  s [62], which is an order of magnitude smaller than  $t_0$  values in Fig. 3(d). Furthermore, the initial diffusion-limited aggregation should not depend significantly on the aggregation strength between particles. Thus, we hypothesize that aggregation interactions can destabilize initial gel structure formed by flexible RBCs, which leads to structure rearrangement and the apparition of fluid-filled cracks. Interestingly,  $t_0$  seems to have little or no effect on the sedimentation velocity. Note that our  $t_0$  measurements saturate at around 1500 s for fibrinogen concentrations larger than about 100 mg/dl, which is likely the minimal time required for the rearrangement of initial cell network.

## B. Microscopic cellular structures

### 1. 2D structures of sedimented RBCs

Sedimentation speed should directly correlate with the permeability of erythrocyte gel, which can be characterized by the size of voids (or pores) between the cells. In experiments, it is difficult to image such voids in 3D within an ESR tube filled with blood at high hematocrit. Therefore, to assess the dependence of pore sizes within aggregated erythrocyte structures on the attraction strength, we turned to a reduced quasi-2D experiment, in which a small amount of erythrocytes is allowed to settle to the bottom of a pillbox-shaped microscope chamber, as described in Sec. III B 1. Typical resulting gel conformations are presented in Fig. 4. An increase in sedimented gel porosity is also clearly visible, which shows that erythrocytes form long rouleaux structures in strongly aggregating media (i.e., at high fibrinogen concentrations).

Figure 5 shows average pore sizes, defined as the square root of the pores area, as a function of fibrinogen concentration. An increase in the pore size with increasing attraction strength is in qualitative agreement with the hypothesis that the parameter  $R$  should increase with the fibrinogen concentration. Although the total 2D pore area then increases because more cells are seen from the side when incorporated in a rouleau, while most of the cells lie flat at the bottom of the container in Fig. 4(a). This is schematized as insets in Figs. 4(a) and 4(c) for more clarity. Note that the data for pore sizes in Fig. 5 exhibit a substantial deviation for various donors, summarized through the error bars showing standard deviation for the measured average size of various samples. Such donor dependency indicates that erythrocyte properties might also affect the magnitude of void sizes. This is not unexpected, as the properties of percolating gel network are known to strongly depend on the underlying geometrical and dimensional properties of suspended particles [17,19,41].

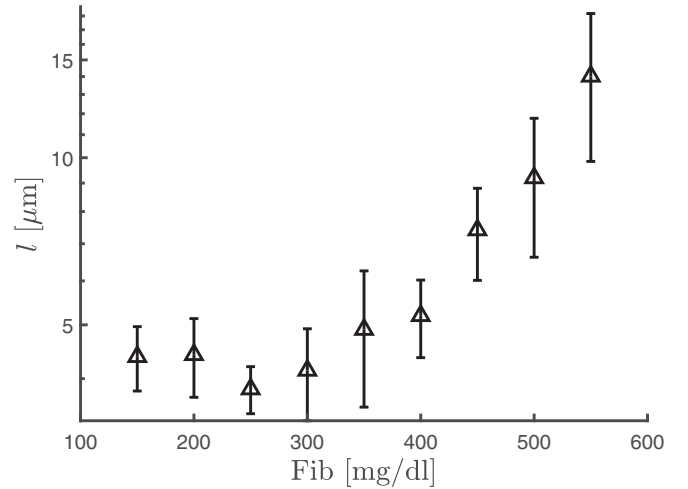


FIG. 5. Mean pore sizes within a quasi-2D percolating network of erythrocytes at the bottom of the observation chamber as a function of fibrinogen concentration in PBS. A trend of increasing pore size with increasing fibrinogen concentration is observed at fibrinogen concentrations above 300 mg/dl. The bars represent standard deviations of the average values measured in various samples from different donors.

Moreover, the quasi 2D-experiments are unlikely to reproduce the quantitative behavior of 3D gel structures. Indeed, the dimension of the system is known to modify the properties of percolating networks [17,19,41], and the presence of a solid wall also likely modifies the obtained structures, due to the trend of the cells to lie flat at the bottom surface. Thus, numerical simulations currently provide the most straightforward way to analyze the bulk structure of erythrocyte suspension during sedimentation.

### 2. Simulations of erythrocyte sedimentation

To understand the relation between microstructural properties of a RBC suspension and its sedimentation, flow simulations are performed for various hematocrits and aggregation interactions, as described in Sec. III B 2. Characteristic simulation snapshots for three attraction strengths  $\epsilon$ , corresponding to three different fibrinogen concentrations, are shown in Figs. 6(a)–6(c). In order to obtain a reasonable computation time, we used volume fractions of 0.25 and 0.35, which are smaller than characteristic values in experiments, but still produce percolating aggregates [20]. The snapshots clearly demonstrate that an increase in  $\epsilon$  leads to stronger clustering of RBCs and larger aggregates. Geometrical analysis of these structures (see Sec. III B 2 for details) allows the extraction of the permeability coefficient  $k$  and the average pore size  $\langle l \rangle$ . Figure 6(d) presents the permeability coefficient which increases with increasing interaction strength  $\epsilon$ , at least in the range of physiological attractive interactions. The characteristic pore size  $\langle l \rangle$  in Fig. 6(e) also consistently increases with the interaction strength.

An increase in the permeability of the erythrocyte gel with increasing pore size is explicitly shown in Fig. 6(f). More importantly, the dependence of  $k$  on  $\langle l \rangle$  is nearly quadratic (i.e.,

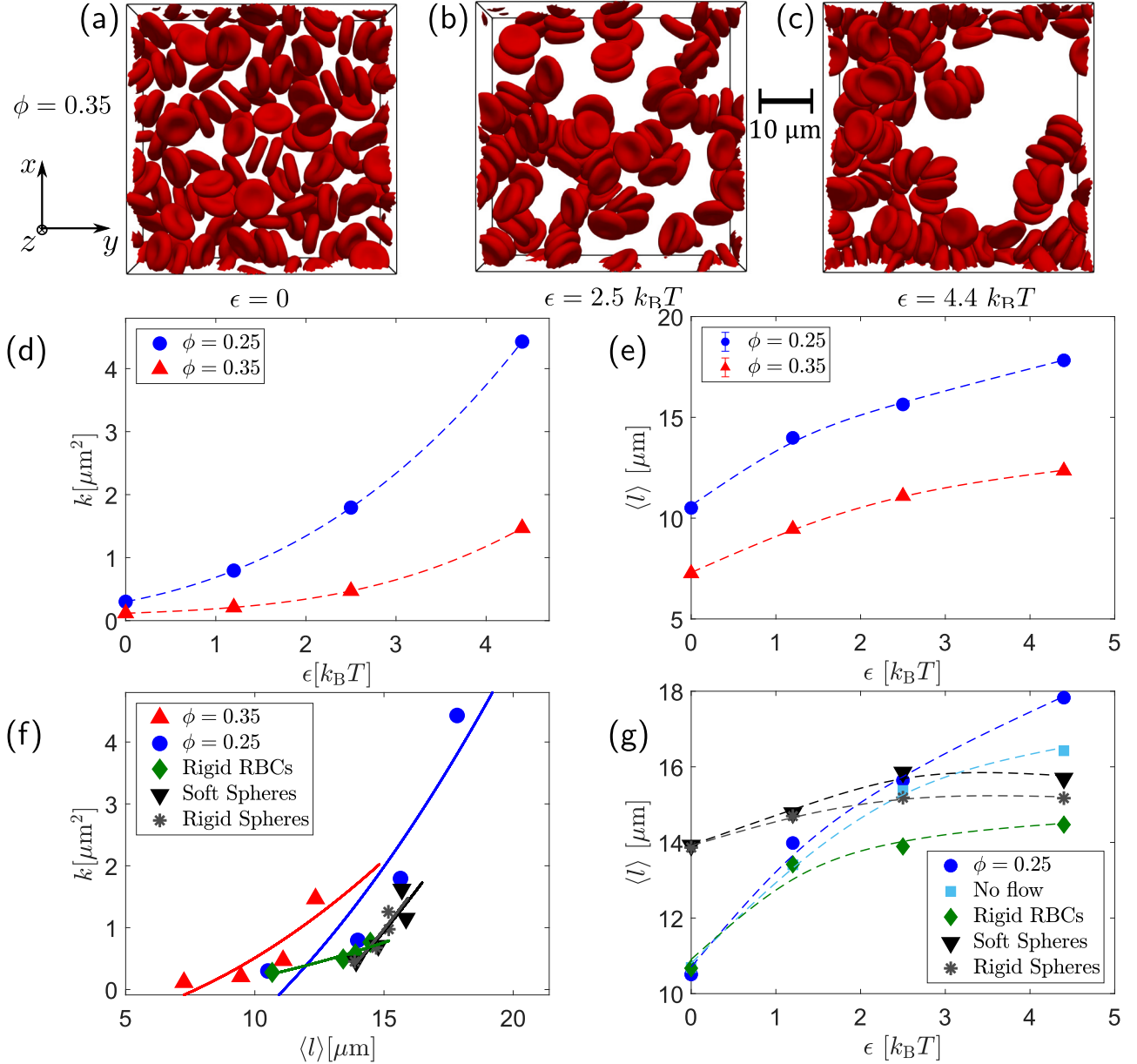


FIG. 6. Effect of interaction strength on the structure and permeability of erythrocyte aggregates from simulations. (a–c) Gelation process from hydrodynamic simulations for different interaction strengths  $\epsilon = \{0, 2.5, 4.4\} k_B T$ . All snapshots are for volume fraction  $\phi = 0.35$  and show a 10- $\mu\text{m}$ -thick layer in  $z$  with a cross section of  $50 \mu\text{m} \times 50 \mu\text{m}$  in  $x$ - $y$ . (d) Permeability coefficient, computed as  $k = (1 - \phi)v\eta/\frac{\partial P}{\partial z}$ , as a function of the interaction strength  $\epsilon$ . The data are displayed for two different hematocrits, and the lines are a guide to the eye. (e) The average pore size  $\langle l \rangle$  from simulations for varying interaction strength  $\epsilon$ . Errors on the average are typically smaller than the symbol sizes. The corresponding distributions of pore sizes are shown in Supplemental Fig. 5 [58]. The lines are a guide to the eye. (f) Permeability coefficient  $k$  as a function of the mean pore size  $\langle l \rangle$  obtained by varying the interaction strength. The lines are quadratic fits ( $k = A + B\langle l \rangle^2$  with  $A$  and  $B$  being fit parameters), which follow the scaling in the Carman-Kozeny relationship ( $k \propto \alpha^2$ ). Except for the data points marked by upward triangles, all data were generated with  $\phi = 0.25$ . (g) The average pore size  $\langle l \rangle$  for different suspension conditions, including a static (no flow) case with deformable RBCs and a suspension of rigid RBCs and spherical particles. All curves are for a volume fraction of  $\phi = 0.25$ . The lines are a guide to the eye. Errors on the average are smaller than the symbol sizes.

$k \propto \langle l \rangle^2$ ), which is consistent with the Carman-Kozeny relationship used in the theoretical model (see Sec. II and the joint letter [20]). In agreement with experimental observations, the increase in the pore size is related to the formation of long network-like rouleaux aggregates (see Fig. 4). This argument is also consistent with distributions of  $l$  (see Supplemental

Fig. 5 [58]) which show that an increasing interaction strength mainly leads to an increase in the number of large pores within the gel network. The combination of these observations explain how an increase in fibrinogen concentration during inflammation results in a faster collapse (or sedimentation) of the erythrocyte gel. Indeed, they show that an increase of



erythrocytes attraction leads to a higher permeability through geometrical effects, which are then responsible for the higher sedimentation rate. This then reconciles the usual diagnostic explanation with the gel-collapse model.

In addition to the effect of interaction strength on the size of pores within erythrocyte gel, it is interesting to look at the importance of fluid stresses, cell elasticity, and cell shape for sedimentation. Figure 6(g) presents average pore sizes for the cases with no fluid flow and for rigidified RBCs and spherical particles. The snapshots of corresponding structures are shown in Supplemental Fig. 6 [58]. The comparison of the  $\phi = 0.25$  curve (with sedimentation flow) with the “static” curve in Fig. 6(g) shows that  $\langle l \rangle$  is only slightly affected by fluid stresses. This is likely due to the fact that fluid flow during sedimentation is generally slow, and thus, the corresponding fluid stresses do not induce significant rearrangements within aggregated network structures. Interestingly, the largest difference in  $\langle l \rangle$  occurs at the largest  $\epsilon$ , which suggests that structures in highly aggregating media might be more fragile. Note that one of the limitations of our simulations is a relatively small simulation domain, since aggregated structures may have differences in stability over different length scales.

We also consider for comparison the case of rigidified cells, whose bending and shear moduli of the membrane are set to be ten times larger than those of normal RBCs. The results in Fig. 6(g) demonstrate that even though  $\langle l \rangle$  still increases with  $\epsilon$  for rigidified RBCs, the slope of the curve nearly vanishes at large enough attraction strength. This means that for  $\epsilon \gtrsim k_B T$ , membrane deformability plays a dominant role for the pore size and the speed of sedimentation. For instance, this is likely the main reason why the ESR is very low in acanthocytosis disease, where an increased rigidity and shape changes in RBCs are frequently observed [63]. For comparison, Fig. 6(g) also presents pore sizes for suspensions of both soft and rigid spheres during sedimentation. In these simulations, we observed that the spheres form aggregates which percolate ( $p_\phi > 0.9$ ) for  $\epsilon \geq 1.2$ . At low  $\epsilon$ ,  $\langle l \rangle$  for the suspension of spheres is larger than that for RBCs. As soon as  $\epsilon > 0$  increases, the average pore size quickly saturates and becomes independent of  $\epsilon$ , which is consistent with the effect of particle rigidity on sedimentation discussed above. The dependence on the aggregation energy is slightly smaller for the rigid than for the soft spheres. This supports the idea that both shape and rigidity influence the structure of the network. As shown by the permeability reported in Fig. 6(f), the increase in average pore size leads to faster sedimentation. Interestingly, when the permeability of the various shapes is shown as a function of the average pore size  $\langle l \rangle$ , the data obtained with a constant hematocrit  $\phi = 0.25$  have fairly comparable values. This supports our assumption that the average pore size is the appropriate parameter to describe the dynamic properties of the percolated network. Furthermore, the small variation of  $\langle l \rangle$  as a function of  $\epsilon$  is in agreement with properties of rigid-particle suspensions, such that spherical particles form fractal aggregates whose fractal dimensions depend on the aggregation regime, but not on the magnitude of the attractive force

[64–66]. As a result, the dependence of ESR on fibrinogen concentration for erythrocyte suspensions is governed by the combination of anisotropic shape and membrane flexibility of these cells.

## V. SUMMARY AND CONCLUSIONS

We have shown with a combination of experiments, theory, and simulations that an increase in erythrocyte sedimentation velocity due to an increase in aggregation interactions between erythrocytes can be explained through the formation of a gel structure, its permeability characteristics, and collapse dynamics. Suspensions of spherical and rigid particles show much less sensitivity of the sedimentation speed to the attraction strength, demonstrating that RBC anisotropy and flexibility govern the structure of RBC aggregates and their sedimentation behavior. These results are consistent with the erythrocyte gel hypothesis and the theoretical model of sedimentation we introduced [20].

Our measurements also demonstrate an unexpected dependence of the delay time  $t_0$  before sedimentation starts on the aggregation strength. In particular,  $t_0$  decreases with increasing  $\epsilon$ , so that the sedimentation process starts faster. This behavior is exactly opposite for suspensions of rigid particles, where attractive interactions stabilize the gel and delay its sedimentation. We hypothesize that RBC membrane flexibility determines  $t_0$ , as supported by the additional data in the Supplemental Material [58] and reduces erythrocyte gel stability at large interaction strengths. Nevertheless, these differences in the sedimentation of suspensions of soft and rigid particles require further investigation.

In conclusion, our results show that erythrocyte suspensions should be considered as soft-particle gels, in contrast to the common proposition of the sedimentation as large, separate cell aggregates. Thus, the structure and dynamics of erythrocyte suspensions can be analyzed and characterized by same physical tools and as many other particle suspensions with a high volume fraction. This observation opens up ways to develop diagnostic applications in diseases (e.g., acanthocytosis) involving some modification of erythrocyte properties, as suggested in a previous study [63]. Importantly, RBC anisotropy and flexibility place these suspensions into a class of soft-particle systems whose sedimentation behavior and comprehensive theoretical description are still open physical questions which have to be addressed in future research.

## ACKNOWLEDGMENTS

This work was supported by the research unit FOR 2688 - Wa1336/12 of the German Research Foundation, and by the Marie Skłodowska-Curie Grant Agreement No. 860436-EVIDENCE. T.J. and C.W. acknowledge funding from French German University (DFH/UFA). We gratefully acknowledge the computing time granted through JARA-HPC on the supercomputer JURECA at Forschungszentrum Jülich.

- [1] I. Lapić, A. Padoan, D. Bozzato, and M. Plebani, Erythrocyte sedimentation rate and C-reactive protein in acute inflammation: Meta-analysis of diagnostic accuracy studies, *Am. J. Clin. Pathol.* **153**, 14 (2020).
- [2] I. Lapić, D. Rogić, and M. Plebani, Erythrocyte sedimentation rate is associated with severe coronavirus disease 2019 (COVID-19): A pooled analysis, *Clin. Chem. Lab. Med. (CCLM)* **58**, 1146 (2020).
- [3] B. H. McCabe, A brief history of the erythrocyte sedimentation rate, *Lab. Med.* **16**, 177 (1985).
- [4] M. A. Taye, Sedimentation rate of erythrocyte from physics prospective, *Eur. Phys. J. E* **43**, 1 (2020).
- [5] O. Baskurt, B. Neu, and H. J. Meiselman, *Red Blood Cell Aggregation* (CRC Press, Boca Raton, FL, 2011).
- [6] R. Smallwood, W. Tindale, and E. Trowbridge, The physics of red cell sedimentation, *Phys. Med. Biol.* **30**, 125 (1985).
- [7] C. Puccini, D. Stasiw, and L. Cerny, The erythrocyte sedimentation curve: A semi-empirical approach, *Biorheology* **14**, 43 (1977).
- [8] K. L. Dorrington and B. S. Johnston, The erythrocyte sedimentation rate time curve: Critique of an established solution, *J. Biomech.* **16**, 99 (1983).
- [9] J. V. d. C. Sousa, M. N. dos Santos, L. Magna, and E. C. de Oliveira, Validation of a fractional model for erythrocyte sedimentation rate, *Comput. Appl. Math.* **37**, 6903 (2018).
- [10] J. Rouwhorst, P. Schall, C. Ness, T. Blijdenstein, and A. Zaccone, Nonequilibrium master kinetic equation modeling of colloidal gelation, *Phys. Rev. E* **102**, 022602 (2020).
- [11] H. Guo, S. Ramakrishnan, J. L. Harden, and R. L. Leheny, Gel formation and aging in weakly attractive nanocolloid suspensions at intermediate concentrations, *J. Chem. Phys.* **135**, 154903 (2011).
- [12] L. J. Teece, J. M. Hart, K. Y. N. Hsu, S. Gilligan, M. A. Faers, and P. Bartlett, Gels under stress: The origins of delayed collapse, *Colloids Surf. A* **458**, 126 (2014).
- [13] R. Buscall, T. H. Choudhury, M. A. Faers, J. W. Goodwin, P. A. Luckham, and S. J. Partridge, Towards rationalising collapse times for the delayed sedimentation of weakly-aggregated colloidal gels, *Soft Matter* **5**, 1345 (2009).
- [14] V. Gopalakrishnan, K. S. Schweizer, and C. Zukoski, Linking single particle rearrangements to delayed collapse times in transient depletion gels, *J. Phys.: Condens. Matter* **18**, 11531 (2006).
- [15] P. Padmanabhan and R. Zia, Gravitational collapse of colloidal gels: Non-equilibrium phase separation driven by osmotic pressure, *Soft Matter* **14**, 3265 (2018).
- [16] P. Bartlett, L. J. Teece, and M. A. Faers, Sudden collapse of a colloidal gel, *Phys. Rev. E* **85**, 021404 (2012).
- [17] S. Manley, J. M. Skotheim, L. Mahadevan, and D. A. Weitz, Gravitational Collapse of Colloidal Gels, *Phys. Rev. Lett.* **94**, 218302 (2005).
- [18] C. Derac, D. Senis, L. Talini, and C. Allain, Rapid settling of a colloidal gel, *Phys. Rev. E* **67**, 062401 (2003).
- [19] C. Allain, M. Cloitre, and M. Wafra, Aggregation and Sedimentation in Colloidal Suspensions, *Phys. Rev. Lett.* **74**, 1478 (1995).
- [20] A. Darras, A. K. Dasanna, T. John, G. Gompper, L. Kaestner, D. A. Fedosov, and C. Wagner, Erythrocyte Sedimentation: Collapse of a High-Volume-Fraction Soft-Particle Gel, *Phys. Rev. Lett.* **128**, 088101 (2022).
- [21] A. Pribush, D. Meyerstein, and N. Meyerstein, The mechanism of erythrocyte sedimentation. Part 1: Channeling in sedimenting blood, *Colloids Surf., B* **75**, 214 (2010).
- [22] G. M. Channell, K. T. Miller, and C. F. Zukoski, Effects of microstructure on the compressive yield stress, *AIChE J.* **46**, 72 (2000).
- [23] M. L. Kilfoil, E. E. Pashkovski, J. A. Masters, and D. Weitz, Dynamics of weakly aggregated colloidal particles, *Philos. Trans. R. Soc. London A* **361**, 753 (2003).
- [24] S. W. Kamp and M. L. Kilfoil, Universal behaviour in the mechanical properties of weakly aggregated colloidal particles, *Soft Matter* **5**, 2438 (2009).
- [25] A. D. Dinsmore, V. Prasad, I. Y. Wong, and D. A. Weitz, Microscopic Structure and Elasticity of Weakly Aggregated Colloidal Gels, *Phys. Rev. Lett.* **96**, 185502 (2006).
- [26] S. B. Lindström, T. E. Kodger, J. Sprakel, and D. A. Weitz, Structures, stresses, and fluctuations in the delayed failure of colloidal gels, *Soft Matter* **8**, 3657 (2012).
- [27] S. E. Bedell and B. T. Bush, Erythrocyte sedimentation rate. From folklore to facts, *Am. J. Med.* **78**, 1001 (1985).
- [28] A. Kratz, M. Plebani, M. Peng, Y. Lee, R. McCafferty, S. Machin, and I. C. for Standardization in Haematology (ICSH), ICSH recommendations for modified and alternate methods measuring the erythrocyte sedimentation rate, *Int. J. Lab. Hematol.* **39**, 448 (2017).
- [29] K. Terzaghi, *Erdbaumechanik auf bodenphysikalischer Grundlage* (Leipzig u. Wien, F. Deuticke., 1925).
- [30] P. C. Carman, Permeability of saturated sands, soils and clays, *J. Agric. Sci.* **29**, 262 (1939).
- [31] T. Ozgumus, M. Mobedi, and U. Ozkol, Determination of Kozeny constant based on porosity and pore to throat size ratio in porous medium with rectangular rods, *Eng. Appl. Comput. Fluid Mech.* **8**, 308 (2014).
- [32] A. W. J. Heijs and C. P. Lowe, Numerical evaluation of the permeability and the Kozeny constant for two types of porous media, *Phys. Rev. E* **51**, 4346 (1995).
- [33] P. Xu and B. Yu, Developing a new form of permeability and Kozeny–Carman constant for homogeneous porous media by means of fractal geometry, *Adv. Water Resour.* **31**, 74 (2008).
- [34] N. Norouzi, H. C. Bhakta, and W. H. Grover, Sorting cells by their density, *PLoS ONE* **12**, e0180520 (2017).
- [35] R. J. Trudnowski and R. C. Rico, Specific gravity of blood and plasma at 4 and 37 °C, *Clin. Chem.* **20**, 615 (1974).
- [36] M. Brust, O. Aouane, M. Thiébaud, D. Flormann, C. Verdier, L. Kaestner, M. Laschke, H. Selmi, A. Benyoussef, T. Podgorski *et al.*, The plasma protein fibrinogen stabilizes clusters of red blood cells in microcapillary flows, *Sci. Rep.* **4**, 1 (2014).
- [37] D. Flormann, E. Kuder, P. Lipp, C. Wagner, and L. Kaestner, Is there a role of C-reactive protein in red blood cell aggregation? *Int. J. Lab. Hematol.* **37**, 474 (2015).
- [38] K. Lee, M. Kinnunen, M. D. Khokhlova, E. V. Lyubin, A. V. Priezhev, I. Meglinski, and A. A. Fedyanin, Optical tweezers study of red blood cell aggregation and disaggregation in plasma and protein solutions, *J. Biomed. Opt.* **21**, 035001 (2016).
- [39] H. J. Issaq, Z. Xiao, and T. D. Veenstra, Serum and plasma proteomics, *Chem. Rev.* **107**, 3601 (2007).
- [40] Z. Yu, G. Kastenmüller, Y. He, P. Belcredi, G. Möller, C. Prehn, J. Mendes, S. Wahl, W. Roemisch-Margl, U. Ceglarek *et al.*,

- Differences between human plasma and serum metabolite profiles, *PLoS ONE* **6**, e21230 (2011).
- [41] D. Stauffer and A. Aharony, *Introduction to Percolation Theory* (CRC Press, Boca Raton, FL, 2018).
- [42] H. Noguchi and G. Gompper, Shape transitions of fluid vesicles and red blood cells in capillary flows, *Proc. Natl. Acad. Sci. USA* **102**, 14159 (2005).
- [43] D. A. Fedosov, B. Caswell, and G. E. Karniadakis, A multiscale red blood cell model with accurate mechanics, rheology, and dynamics, *Biophys. J.* **98**, 2215 (2010).
- [44] D. A. Fedosov, B. Caswell, and G. E. Karniadakis, Systematic coarse-graining of spectrin-level red blood cell models, *Comput. Meth. Appl. Mech. Eng.* **199**, 1937 (2010).
- [45] W. Linss, C. Pilgrim, and H. Feuerstein, How thick is the glycocalyx of human erythrocytes? *Acta Histochem.* **91**, 101 (1991).
- [46] N. M. Geekiyanage, M. A. Balanant, E. Sauret, S. Saha, R. Flower, C. T. Lim, and Y. Gu, A coarse-grained red blood cell membrane model to study stomatocyte-discocyte-echinocyte morphologies, *PLoS ONE* **14**, e0215447 (2019).
- [47] D. A. Fedosov, W. Pan, B. Caswell, G. Gompper, and G. E. Karniadakis, Predicting human blood viscosity in silico, *Proc. Natl. Acad. Sci. USA* **108**, 11772 (2011).
- [48] P. Ermolinskiy, A. Lugovtsov, F. Yaya, K. Lee, L. Kaestner, C. Wagner, and A. Priezhev, Effect of red blood cell aging in vivo on their aggregation properties in vitro: Measurements with laser tweezers, *Appl. Sci.* **10**, 7581 (2020).
- [49] P. Español and M. Revenga, Smoothed dissipative particle dynamics, *Phys. Rev. E* **67**, 026705 (2003).
- [50] K. Müller, D. A. Fedosov, and G. Gompper, Smoothed dissipative particle dynamics with angular momentum conservation, *J. Comput. Phys.* **281**, 301 (2015).
- [51] Z. Varga, G. Wang, and J. Swan, The hydrodynamics of colloidal gelation, *Soft Matter* **11**, 9009 (2015).
- [52] Z. Varga, J. L. Hofmann, and J. W. Swan, Modelling a hydrodynamic instability in freely settling colloidal gels, *J. Fluid Mech.* **856**, 1014 (2018).
- [53] A. Razali, C. J. Fullerton, F. Turci, J. E. Hallett, R. L. Jack, and C. P. Royall, Effects of vertical confinement on gelation and sedimentation of colloids, *Soft Matter* **13**, 3230 (2017).
- [54] E. A. Evans and R. Skalak, *Mechanics and Thermodynamics of Biomembranes* (CRC Press, Boca Raton, FL, 1980).
- [55] E. A. Evans, Bending elastic modulus of red blood cell membrane derived from buckling instability in micropipet aspiration tests, *Biophys. J.* **43**, 27 (1983).
- [56] M. Dao, C. T. Lim, and S. Suresh, Mechanics of the human red blood cell deformed by optical tweezers, *J. Mech. Phys. Solids* **51**, 2259 (2003).
- [57] M. Peltomäki and G. Gompper, Sedimentation of single red blood cells, *Soft Matter* **9**, 8346 (2013).
- [58] See Supplemental Material at <http://link.aps.org/supplemental/10.1103/PhysRevE.105.024610> for Supplemental Materials. They contain a short discussion of the influence of cell rigidity on the delay time, a discussion of the influence of aggregation energy on the percolation, Supplemental Fig. 3 (illustration of pore sizes determination by numerical simulations), Supplemental Fig. 4 (hole size PDF from simulations), Supplemental Fig. 5 (hole size PDF), Supplemental Fig. 6 (structures obtained in various conditions), and Supplemental Movie S1/H40ImageJ.avi (illustrative movie generated from numerical simulations).
- [59] M. Mathew, T. Schilling, and M. Oettel, Connectivity percolation in suspensions of hard platelets, *Phys. Rev. E* **85**, 061407 (2012).
- [60] I. Safeukui, P. A. Buffet, G. Deplaine, S. Perrot, V. Brousse, A. Sauvanet, B. Aussilhou, S. Dokmak, A. Couvelard, D. Cazals-Hatem *et al.*, Sensing of red blood cells with decreased membrane deformability by the human spleen, *Blood Adv.* **2**, 2581 (2018).
- [61] A. M. Forsyth, J. Wan, W. D. Ristenpart, and H. A. Stone, The dynamic behavior of chemically “stiffened” red blood cells in microchannel flows, *Microvasc. Res.* **80**, 37 (2010).
- [62] W. Russel, D. Saville, and W. Schowalter, *Colloidal Dispersions* (Cambridge University Press, Cambridge, 1989).
- [63] A. Darras, K. Peikert, A. Rabe, F. Yaya, G. Simionato, T. John, A. K. Dasanna, S. Buvalyy, J. Geisel, A. Hermann *et al.*, Acanthocyte sedimentation rate as a diagnostic biomarker for neuroacanthocytosis syndromes: Experimental evidence and physical justification, *Cells* **10**, 788 (2021).
- [64] L. D. Gelb, A. L. Graham, A. M. Mertz, and P. H. Koenig, On the permeability of colloidal gels, *Phys. Fluids* **31**, 021210 (2019).
- [65] S. K. Friedlander, *Smoke, Dust, and Haze: Fundamentals of Aerosol Dynamics* (Oxford University Press, Oxford, 2000).
- [66] D. Senis, L. Gorre-Talini, and C. Allain, Systematic study of the settling kinetics in an aggregating colloidal suspension, *Eur. Phys. J. E* **4**, 59 (2001).